Breakdown characteristics of high pressure xenon lamps

2009 J. Phys. D: Appl. Phys. 42 185208

(http://iopscience.iop.org/0022-3727/42/18/185208)

J. Phys. D: Appl. Phys. **42** (2009) 185208 (12pp) doi:10.1088/0022-3727/42/18/185208

Breakdown characteristics of high pressure xenon lamps

M Wendt[1,4], S Peters[2], D Loffhagen[1], A Kloss[3] and M Kettlitz[1]

[1] INP Greifswald, Felix-Hausdorff-Str. 2, 17489 Greifswald, Germany
[2] Physikalisch-Technische Bundesanstalt, Bundesallee 100, 38116 Braunschweig, Germany
[3] OSRAM GmbH, Research Light Sources, SIGMA Technopark Augsburg, Werner-von-Siemens-Str. 6, 86159 Augsburg, Germany

E-mail: wendt@inp-greifswald.de

Received 5 June 2009, in final form 30 July 2009
Published 4 September 2009
Online at stacks.iop.org/JPhysD/42/185208

Abstract
An investigation of the breakdown of high intensity discharge (HID) lamps filled with xenon at pressures from 0.1 to 5 bar is presented. Three power supplies were used in order to provide voltage rates of increase covering about four orders of magnitude from 5 mV ns^{-1} to 100 V ns^{-1}, the latter being typical for electronic ballasts driving commercial HID lamps. Customized lamps ensure a volume breakdown between the tungsten tip electrodes of the lamp. Voltage and current waveforms were measured by means of electrical probes and the transient optical radiation was captured by a fast camera system. The breakdown voltage increases with growing pressure and voltage rate up to several 10 kV. Additional UV illumination decreases the breakdown voltage and reduces its mean variation. The experimental results were reproduced with good agreement by a fluid model taking into account the electron energy balance. The model shows an ionization front propagating towards the cathode. The front moves due to continuous field compression and relies on electron avalanches initiated by secondary electrons at the cathode.

(Some figures in this article are in colour only in the electronic version)

1. Introduction

High intensity discharge lamps (HID) have found widespread use in applications requiring high efficacy, high quality colour rendering, high lumen output from a small active volume and a long service life. One such application is the automotive head lamp. An additional demand of this application is the immediate light output after switching-on. It is met by filling HID head lamps with metal halides and xenon at pressures of several bars so that xenon provides the lumen output of the lamp during its warm-up period [1, 2]. However, the high pressures in combination with the high voltage rates $\mathrm{d}U/\mathrm{d}t$ delivered by commercial electronic ballasts lead to breakdown voltages of several 10 kV. The aim of this work is to contribute to the understanding of the basic processes leading to these high breakdown voltages.

The reduction in the breakdown voltage is one goal of HID design and can be achieved by several means. Using a two-dimensional model, Lay *et al* [3] demonstrated that suitably placed extra electrodes facilitate the breakdown of lamps filled with argon and mercury. Kushner *et al* demonstrated in experiments [4] and by modelling [5] that admixtures of xenon can significantly reduce the breakdown voltage of argon filled HID lamps due to particular ionization kinetics. Beckers *et al* [6] reported that ac voltages reduce the breakdown voltage with respect to those obtained by pulsed voltages.

Due to the high voltages the electron avalanches in commercial HID lamps pass the Raether–Meek criterion [7] and form filamentary, streamer-like ionizing channels. Czichy *et al* [8] observed that these channels can originate from the cathode and the anode, and that they can branch and travel through the gas volume as well as along the inner wall of the arc vessel. The authors found that breakdown events with high and low breakdown voltages are associated with volume and wall propagating plasma channels, respectively. Sobota *et al* [9] found cathode-directed ionizing channels during the

[4] Author to whom any correspondence should be addressed.

breakdown of argon and reported that these channels have higher velocities when propagating along the wall than when propagating through the gas volume. The propagation velocity of the ionizing channels was found to increase with decreasing pressure, increasing dU/dt and decreasing distance to the cathode.

Fluid models of streamers and ionization waves usually comprise the Poisson equation, species continuity and momentum balance equations. Non-local effects can be treated by including the electron energy balance equation [5, 10–12] or, alternatively, by using particle-in-cell models as applied to streamers in [13]. For high momentum dissipation frequencies the electron momentum balance in fluid models can be replaced by the drift–diffusion approximation. For high energy dissipation rates the electrons reach a quasi steady state in which their energy distribution function is only a function of the local electric field. In this case, the so-called local field approximation, the electron energy balance is omitted and the electron transport and rate coefficients are evaluated as functions of the local electric field. A comparison of different numerical approaches to models using both these approximations when applied to streamers was presented by Ducasse *et al* [14]. A detailed analysis of a fluid model of streamers with constant transport parameters was given by Ebert *et al* [15]. More advanced models include photoionization in order to investigate its influence on propagation speed and branching behaviour [16–21] or detailed reaction schemes in order to estimate reactive species densities [22, 23]. Due to their environmental relevance many investigations were performed on streamers in air propagating in the upper atmosphere [24, 25] or at ambient pressure as in e.g. [26, 27].

The current investigation focuses on the volume breakdown of HID lamps filled with pure xenon. In particular, the dependence of the breakdown voltage on pressure, voltage rate and additional UV radiation has been investigated. The experiments cover pressures from 0.1 to 5 bar and voltage rates from 5 mV ns^{-1} to 100 V ns^{-1}. Specially designed model lamps exclude a wall-assisted breakdown in the experiments so that the experimental results can clearly be attributed to a volume breakdown in contrast to the experiments presented by Beckers [6] and Czichy [8] where both types of breakdown occur. The experimental results are compared with results of model calculations. The fluid model of the plasma consists of the coupled solution of the system of continuity equations of the relevant species, the electron energy balance, the Poisson equation and the electrical circuit equation. The particle and energy balance equations have been solved in time and one spatial dimension by means of a modern numerical scheme [28, 29]. In the following, the experimental set-up and the main features of the model are described at first and then modelling and experimental results are discussed.

2. Experiment

In conventional HID lamps breakdown is supported by a starting gas, usually some ten millibar of argon resulting in a diffuse breakdown through the volume. For HID lamps with higher filling pressures and small discharge volume the ionizing channels forming during the breakdown are more constricted and can propagate through the gas volume as well as along the walls. An example of such a wall-assisted breakdown of an automotive head lamp filled with xenon ($p \approx 15$ bar) is shown in figure 1.

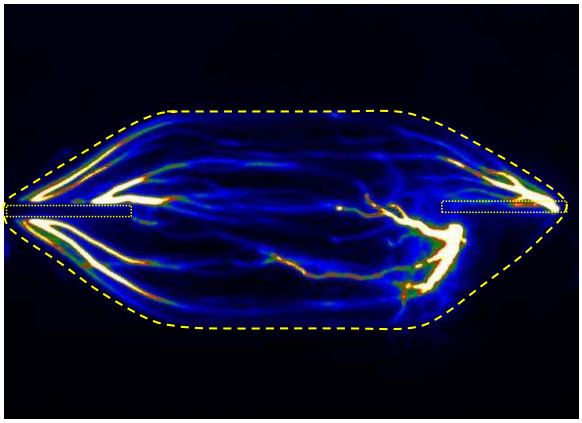

Figure 1. Streamer propagation in an automotive lamp along the walls and in the volume (lamp wall and electrodes are indicated, the intensities are in false colour).

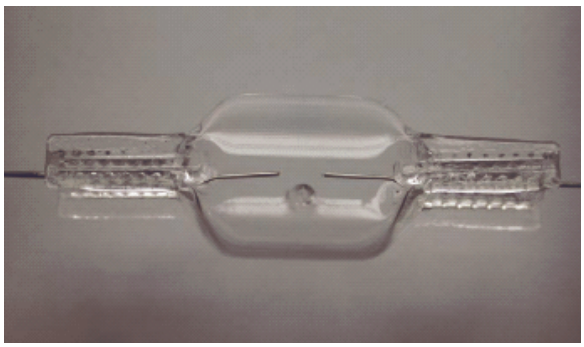

Figure 2. Quartz model lamp ($\varnothing = 24$ mm) with tungsten electrodes ($\varnothing = 0.5$ mm, gap 5 mm).

In order to clearly separate volume and wall-assisted breakdown in the experiments, special model lamps were designed and produced by OSRAM. The employed lamps, depicted in figure 2, consist of a quartz tube with an inner diameter of 24 mm and a length of 30 mm. They are filled with xenon in a pressure range between 0.1 and 5 bar where streamer breakdown appears. The upper limit of the pressure range was given by safety concerns. The lamps have prolonged tungsten electrodes with a length of 14 mm, a diameter of 0.5 mm and a resulting electrode gap d of 5 mm. In a conditioning procedure the electrodes and the gas filling of the lamps were cleaned from traces of residual water and oxygen. An example of the streamer propagation in a model lamp filled with 1 bar xenon is shown in figure 3. Initial experiments verified that in the chosen lamp design, a wall-assisted breakdown does not occur. Images taken simultaneously from the top and from the front side of the lamps showed that the streamer has no contact with the walls during breakdown so that volume breakdown is guaranteed.

The experimental set-up is shown in figure 4. The lamps were placed in a special mount and connected to the power

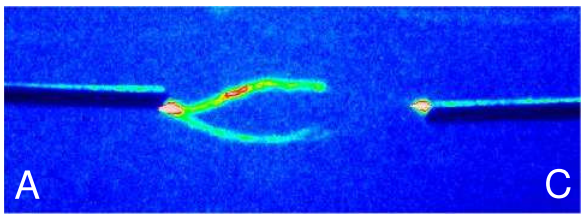

Figure 3. Streamer propagation in the volume in the model lamp with 1 bar Xe, anode (A) on the left and cathode (C) on the right-hand side (the intensities are in false colour).

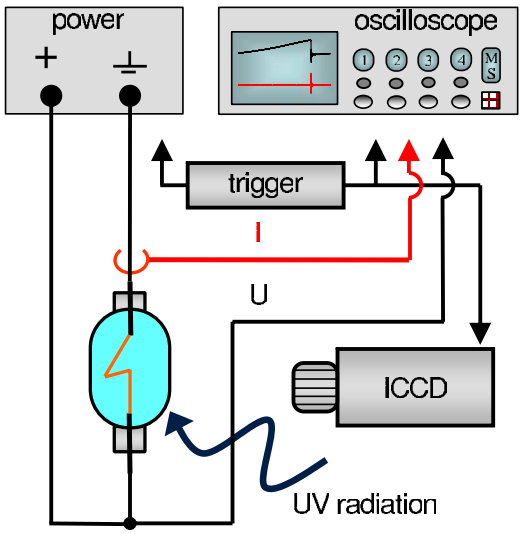

Figure 4. Schematic view of the experimental set-up.

supply. Several power supplies with constant or variable voltage rises were used. For a slow increase an HV capacitor charging power supply (HCK800M-20000, FUG) was used in current limited loading mode charging a capacitor of 10 nF allowing finally rise times down to 0.6 V μs^{-1}. The breakdown process itself is some orders of magnitude faster in the range of nano seconds.

A medium voltage rise of 0.4 V ns^{-1} was produced by an automotive induction coil (KW12V, Bosch). In this case a capacitor of 2 μF was discharged over a part of the induction coil by opening a semiconductor switch creating a high voltage pulse at the end. The fastest rise times of 100 V ns^{-1} were generated by applying the voltage of a charged capacitor of 1 nF to the lamps with the help of a fast high voltage transistor switch (HTS 331-03-LC, Behlke). Equally fast pulses were obtained using an electronic igniter for automotive head lamps (EVG/AM, OSRAM). In all measurements a positive voltage pulse was applied to the powered electrode of the lamps while the second electrode was grounded. Voltage and electrical current were measured by means of fast probes (P6015A, Tektronix, and models 2877 and 2878, Pearson Electronics) and recorded with 500 MHz resolution by a 5 GS s^{-1} real time oscilloscope (TDS 7054, Tektronix).

The spatiotemporal development of the electrical breakdown was observed in the visible spectral range by high speed photography using a framing camera (Imacon468, Headland Photonics). The lamps were imaged to the camera by a special optics. A beam splitter inside the camera spreads

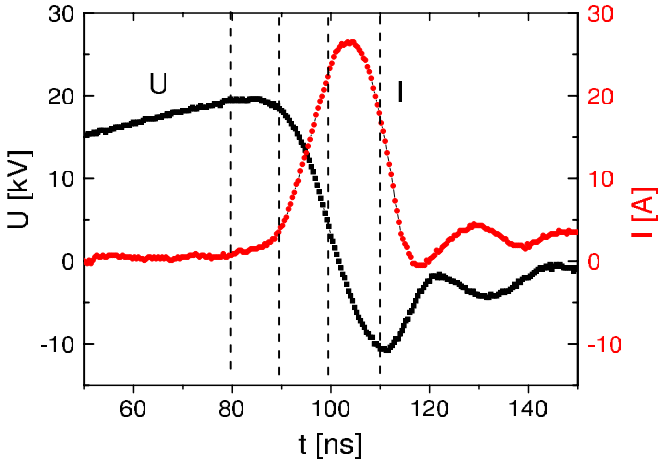

Figure 5. The principle of the measurement is shown for a 3 bar lamp at a voltage rise dU/dt of 100 V ns^{-1}. The breakdown voltage with additional UV radiation is 19.5 kV. The framing camera took pictures as marked in the voltage curve, before and during breakdown.

the light onto four separately intensified CCDs. In this way four independent pictures with high spatial resolution could be recorded allowing exposure times down to 10 ns and programmable delays without any external synchronization of the four CCDs necessary.

A second camera allowing exposure times of 2 ns (iStar, Andor) was used additionally to get an extra picture with smaller exposure time that could be delayed to the other ones. This was useful because the streamer velocity is very high as the calculations show and the propagation time between the electrodes in the lamps is in the nanosecond range.

The power supplies, the cameras and the oscilloscope were synchronized by use of an additional pulse and delay generator (DG535, SI). The delay generator is used to compensate the signal propagation velocities in the cables and gives the initial trigger starting the measurements. For high voltage rises the pre-trigger delivered by the electronic power supply is used as initial trigger.

A low pressure mercury lamp (HNS12, OSRAM) was used to illuminate the model lamps with UV radiation in order to investigate its influence on the breakdown voltage. In most cases it was used as background illumination. In some experiments the UV radiation was focused with a spot size of 1 mm^2 to various parts of the lamp to investigate the spatial dependence of the radiation on breakdown.

The principle of the measurement is shown in figure 5. At the beginning of the breakdown the resistance in the lamp decreases rapidly and current starts to flow leading in turn to a drop in the applied voltage. The maximum voltage was taken as breakdown voltage U_b. The voltage rise dU/dt shown in figure 5 was 100 V ns^{-1}, and the resulting breakdown voltage was 19.5 kV. The framing camera took pictures before and during breakdown as marked in the voltage curve.

An investigation with varied delay time between measurements showed that the conditioning of the gas by the preceding breakdown can have a significant influence on the streamer behaviour. Choosing a pause of 20 s between every

voltage pulse rules out an influence of the repetition rate on the measurements presented below.

Multiple electrical and optical measurements allowed a statistical assessment of the breakdown process. The mean value and the standard deviation of the electrical measurements were calculated from 50 shots of 3 to 5 lamps for each xenon pressure. The combination of electrical values and streamer snap shots gave a general view of the breakdown process.

3. Description of the model

The plasma during the breakdown is strongly out of equilibrium so that the mean electron energy can reach several electron volts while the temperature of ions and neutrals stays around room temperature. The reaction kinetics of the excited states of xenon induced by electron and heavy particle collisions and the formation of excimer molecules has been investigated in e.g. [30–32]. As the focus of this investigation is on the dependence of the breakdown voltage on the circuit parameters, a strongly reduced set of collisional processes is used in this model. In particular, the ionization of excited atomic states and excimer molecules by electron impact and chemi-ionization have not been taken into account. The plasma is described by a time-dependent, spatially one-dimensional fluid model consisting of Poisson's equation, continuity equations for electrons (e), xenon atomic ions (Xe^+) and molecular ions (Xe_2^+) and the energy balance for the electrons. The spatial inhomogeneity is assumed in the x-direction. The transport parameters of the electrons and the rates for collisions involving electrons have been evaluated as functions of the local mean electron energy. The drift–diffusion approximation is used to describe the energy flux of the electron gas and the particle fluxes. Similar models have been applied in e.g. [10, 33–37].

The equation system employed reads

$$\varepsilon_0 \nabla^2 \phi = e\,(n_\mathrm{e} - n_\mathrm{i} - n_\mathrm{m})\,, \tag{1}$$

$$\frac{\partial}{\partial t} n_\mathrm{e} + \nabla\,\Gamma_\mathrm{e} = n_\mathrm{e} N k^\mathrm{io} - n_\mathrm{e} n_\mathrm{i} k^\mathrm{hv} - {n_\mathrm{e}}^2 n_\mathrm{i} \beta^\mathrm{3e} - n_\mathrm{e} n_\mathrm{m} k^\mathrm{dr}, \tag{2}$$

$$\frac{\partial}{\partial t} n_\mathrm{i} + \nabla\,\Gamma_\mathrm{i} = n_\mathrm{e} N k^\mathrm{io} - n_\mathrm{e} n_\mathrm{i} k^\mathrm{hv} - {n_\mathrm{e}}^2 n_\mathrm{i} \beta^\mathrm{3e} - N^2 n_\mathrm{i} \beta^\mathrm{cv}, \tag{3}$$

$$\frac{\partial}{\partial t} n_\mathrm{m} + \nabla\,\Gamma_\mathrm{m} = N^2 n_\mathrm{i} \beta^\mathrm{cv} - n_\mathrm{e} n_\mathrm{m} k^\mathrm{dr}, \tag{4}$$

$$\frac{\partial}{\partial t} u_\mathrm{e} + \nabla\,\Gamma_\mathrm{u} = -\Gamma_\mathrm{e} E - n_\mathrm{e} N \left(P^\mathrm{el} + u^\mathrm{io} k^\mathrm{io} + u^\mathrm{ex} k^\mathrm{ex}\right). \tag{5}$$

Here, ε_0 is the permittivity of free space, e is the elementary charge, $\nabla = \partial/\partial x$, N is the ground state density, ϕ is the potential with the electric field $E = -\nabla\phi$ and n_s and Γ_s are the densities and fluxes of electrons, atomic ions and molecular ions with index s = e, i and m, respectively. The quantities k^io, k^ex, k^hv, k^dr, β^3e, β^cv and P^el are the coefficients for ionization and total excitation of xenon in its ground state by electron impact, the coefficients for radiative recombination of Xe^+, dissociative recombination of Xe_2^+, di-electronic recombination of Xe^+, conversion of Xe^+ to Xe_2^+ and the elastic energy loss of the electrons, respectively. The quantity $u^\mathrm{io} = 12.123\,\mathrm{eV}$ is the ionization energy of xenon and $u^\mathrm{ex} = 8.315\,\mathrm{eV}$ is the energy loss in electron excitation processes. Table 1 summarizes the collisional processes included in this model.

Table 1. Reactions and reaction rates: T_e is the electron temperature in eV.

Reaction	Coefficient	Source
$Xe + e \rightarrow Xe + e$	P^el	a
$Xe + e \rightarrow Xe^* + e$	k^ex	a
$Xe + e \rightarrow Xe^+ + 2\,e$	k^io	a
$Xe^+ + e \rightarrow Xe + h\nu$	$k^\mathrm{hv} = 2.7 \times 10^{-19}\,\mathrm{m^3\,s^{-1}}\,T_\mathrm{e}^{-3/4}$	b
$Xe^+ + 2\,e \rightarrow Xe + e$	$\beta^\mathrm{3e} = 8.6 \times 10^{-39}\,\mathrm{m^6\,s^{-1}}\,T_\mathrm{e}^{-9/2}$	b
$Xe^+ + 2\,Xe \rightarrow Xe_2^+ + Xe$	$\beta^\mathrm{cv} = 3.6 \times 10^{-43}\,\mathrm{m^6\,s^{-1}}$	b
$Xe_2^+ + e \rightarrow Xe + Xe$	$k^\mathrm{dr} = 1.6 \times 10^{-14}\,\mathrm{m^3\,s^{-1}}\,T_\mathrm{e}^{-1/2}$	b

[a] Rate calculated from the solution of the Boltzmann equation.
[b] Data from [7].

In the applied drift–diffusion approximation the particle fluxes read

$$\Gamma_s = -\mathrm{sgn}(z_s)\,b_s n_s \nabla\phi - D_s \nabla n_s, \tag{6}$$

where z_s, b_s and D_s are the charge number, the mobility and the diffusion coefficient of species s. For the ions the mobilities $b_s = b_{s0} \times (273.15\,\mathrm{K}/T) \times (1\,\mathrm{atm}/p)$ with $b_{s0} = 0.5 \times 10^{-4}$ and $0.75 \times 10^{-4}\,\mathrm{m^2\,(V^{-1}s^{-1})}$ for Xe^+ and Xe_2^+, respectively, have been used [38]. The diffusion coefficients are estimated by the Einstein relation $D_s = b_s kT/e$ with the Boltzmann constant k and a gas temperature T of 300 K.

The flux of the energy density is approximated by

$$\Gamma_\mathrm{u} = b_\mathrm{u} u_\mathrm{e} \nabla\phi - D_\mathrm{u} \nabla u_\mathrm{e}, \tag{7}$$

where $b_\mathrm{u} = b_\mathrm{u}^* n_\mathrm{e}/u_\mathrm{e}$ and $D_\mathrm{u} = D_\mathrm{u}^* n_\mathrm{e}/u_\mathrm{e}$. Here, b_u^* and D_u^* are mobility and the diffusion coefficient of the electron energy transport.

Figure 6 shows the rate coefficients k^io and k^ex, the transport coefficients b_e, D_e, b_u^*, D_u^* and the elastic loss term P^el used in this model. They were determined by solving the spatially homogeneous, steady-state Boltzmann equation of the electrons using a modified version of the multi-term solution technique [39] adapted to account for non-conservative electron collision processes [40]. The method determines the rate and transport coefficients and the mean electron energy $u_\mathrm{m} = u_\mathrm{e}/n_\mathrm{e}$ as functions of the reduced field strength E/N. In the mean energy approximation used in this model the coefficients are then evaluated at the local, time-dependent value $u_\mathrm{m}(x,t)$ of the mean electron energy. The momentum transfer cross-section in elastic collisions and the ionization cross-section of xenon ground state atoms by electron impact were taken from Hayashi [41] and Rapp and Englander–Golden [42], respectively. The employed total electron impact excitation cross-section [43] represents excitation of the xenon ground state into any excited state Xe^*.

In order to solve the coupled system of equations (1)–(5) appropriate boundary conditions at the spatial margins have to be employed. At the cathode ($x = 0$) the boundary conditions

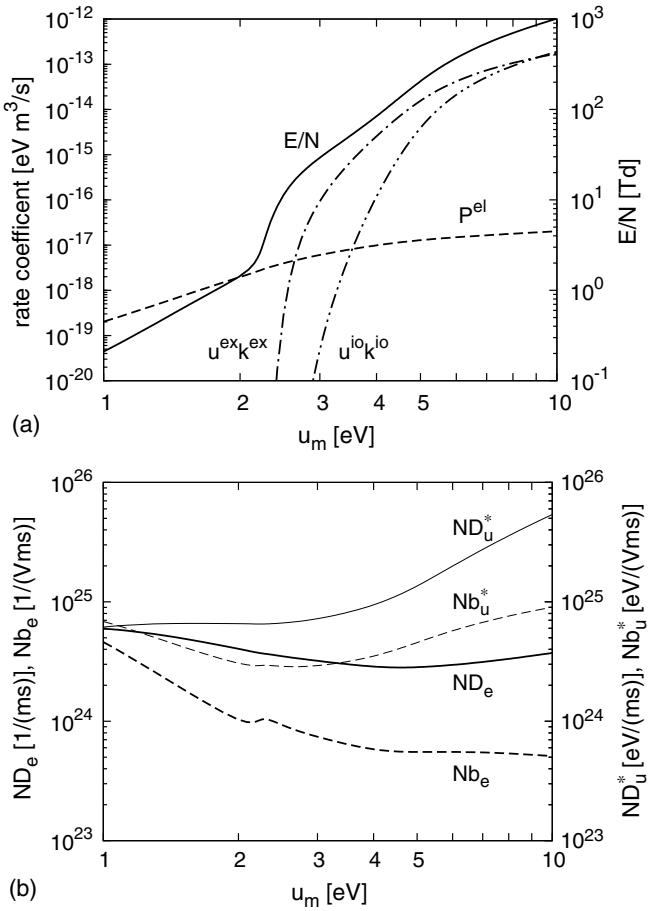

Figure 6. Electric field E, electron energy losses due to elastic collisions P^{el}, excitation $u^{\mathrm{ex}}k^{\mathrm{ex}}$ and ionization $u^{\mathrm{io}}k^{\mathrm{io}}$ (*a*), and mobilities b_{e}, b^*_{u}, and diffusion coefficients D_{e}, D^*_{u} of the electron particle and energy transport, respectively, as a function of the mean electron energy u_{m}.

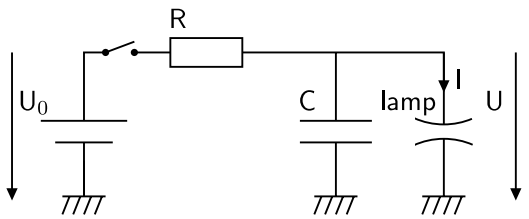

Figure 7. Equivalent circuit with applied voltage $U_0 = 30\,\mathrm{kV}$, external resistor R and stray capacity $C = 1 \times 10^{-11}\,\mathrm{F}$. The electrode distance in the lamp is $d = 5 \times 10^{-3}\,\mathrm{m}$ and the cross-section $A = 1 \times 10^{-4}\,\mathrm{m}^2$.

$\phi = 0$, $\nabla n_{\mathrm{i}} = \nabla n_{\mathrm{m}} = 0$, $u_{\mathrm{m}} = 2\,\mathrm{eV}$ and the secondary emission of electrons by ion impact in the form

$$b_{\mathrm{e}} n_{\mathrm{e}} \nabla\phi = \gamma\Gamma_{\mathrm{i}} + \gamma\Gamma_{\mathrm{m}} \tag{8}$$

with $\gamma = 0.06$ have been used.

At the anode ($x = d$) the conditions $n_{\mathrm{i}} = n_{\mathrm{m}} = 0$ and $\nabla n_{\mathrm{e}} = \nabla u_{\mathrm{e}} = 0$ have been applied. The boundary condition for the potential $\phi(d, t)$ has been obtained from the equation of the electrical circuit. The equivalent circuit representing the coupling to lamp and power supply is depicted in figure 7. The circuit equation reads

$$U_0 = RC\dot{U}(t) + U(t) + RI(t), \tag{9}$$

where U_0 and R are the voltage and the internal resistance of the power supply being considered as an ideal voltage source, U and I are the voltage across and the total current through the lamp and C is the stray capacity. The condition $U(t) = \phi(d, t)$ in combination with the total current

$$I = \epsilon_0 A \frac{\partial}{\partial t}\frac{\partial}{\partial x}\phi - eA\Big(\Gamma_{\mathrm{i}} + \Gamma_{\mathrm{m}} - \Gamma_{\mathrm{e}}\Big) \tag{10}$$

leads to the boundary condition

$$\frac{U_0}{RC} = \frac{\partial}{\partial t}\phi(d,t) + \frac{1}{RC}\phi(d,t) + \epsilon_0\frac{A}{C}\frac{\partial}{\partial t}\frac{\partial}{\partial x}\phi(d,t) - e\frac{A}{C}\Big[\Gamma_{\mathrm{i}}(d,t) + \Gamma_{\mathrm{m}}(d,t) - \Gamma_{\mathrm{e}}(d,t)\Big]. \tag{11}$$

Here A is the effective, electron collecting cross-section of the lamp electrodes. Without charge carriers in the lamp the voltage U develops according to

$$U(t) = U_0\big[1 - \mathrm{e}^{-t/(RC_0)}\big], \tag{12}$$

where $C_0 = C + C_{\mathrm{lamp}}$ and $C_{\mathrm{lamp}} = \varepsilon_0 A/d$ is the vacuum capacity of the lamp. The time derivative of U at $t = 0$, i.e.

$$\mathrm{d}U/\mathrm{d}t = \dot{U}(0) = U_0/(RC_0), \tag{13}$$

is used as a parameter for comparing model and experimental results.

Using the drift–diffusion approximations (6) and (7), the system of equations (1)–(5) can be expressed by the variables ϕ, n_{e}, n_{i}, n_{m} and u_{e}. The continuity and energy balance equations are solved using the cubic interpolated propagation scheme (CIP) given by Yabe and Aoki [28, 29]. The CIP scheme treats differential equations

$$\partial f/\partial t + v(f,t)(\partial f/\partial x) = G(f,t) \tag{14}$$

for quantities f with advection velocity v and inhomogeneous term G by splitting each time step into a non-advective and an advective part. The equations for f and $f' = \partial f/\partial x$ read

$$\partial f/\partial t = G, \tag{15}$$

$$\partial f'/\partial t = \partial G/\partial x - f'\partial v/\partial x \tag{16}$$

in the non-advective step and

$$\partial f/\partial t + v(\partial f/\partial x) = 0, \tag{17}$$

$$\partial f'/\partial t + v(\partial f'/\partial x) = 0 \tag{18}$$

in the advective step. Equations (2)–(5) are transformed into form (14) by setting $v = -\mathrm{sgn}(z_s)\, b_s \nabla\phi$ and $b_{\mathrm{u}} n_{\mathrm{e}}$, respectively, and by introducing G as the sum of the corresponding source terms and of $\mathrm{sgn}(z_s)\nabla(b_s\nabla\phi)n_s + \nabla(D_s\nabla n_s)$ and $-\nabla(b_{\mathrm{u}}\nabla\phi)u_{\mathrm{e}} + \nabla(D_{\mathrm{u}}\nabla u_{\mathrm{e}})$ for the particle densities and the energy density, respectively.

In a time step from $t = t^n$ to $t = t^{n+1}$ the non-advective step for $f = (n_{\mathrm{e}}, n_{\mathrm{i}}, n_{\mathrm{m}}, u_{\mathrm{e}})$ is treated by first solving (15) by

the Crank–Nicolson scheme [44] giving values, say, f^*. Here, the source terms, transport and rate coefficients are evaluated at time t^n while the products $(\nabla^2\phi)n_s$ are linearized. The potential ϕ^* is determined by solving the Poisson equation in parallel to the electron energy balance and the continuity equations. After (15) is solved, f'^* is calculated by applying the finite difference approximation of (16):

$$\frac{f_i'^* - f_i'^n}{\Delta t} = \frac{f_{i+1}^* - f_{i-1}^* - f_{i+1}^n + f_{i+1}^n}{(x_{i+1} - x_{i-1})\Delta t} - f_i'^n \frac{v_{i+1}^n - v_{i-1}^n}{x_{i+1} - x_{i-1}}. \tag{19}$$

Here, $\Delta t = t^{n+1} - t^n$ is the time step and x_i the position of the ith grid point. In equation (19) all quantities except for $f_i'^*$ are known at this point of time.

Secondly, the advective step is solved by shifting f^* and f'^* spatially according to $f_i^{n+1} = f^*(x_i - v\Delta t, t^*)$ and $f_i'^{(n+1)} = f'^*(x_i - v\Delta t, t^*)$. For values $x_i - v\Delta t$ between grid points the cubic interpolation function

$$F_i(x) = \left[(a_i X + b_i)X + f_i'^*\right] X + f_i^* \tag{20}$$

and its spatial derivative

$$F_i'(x) = (3a_i X + 2b_i)\, X + f_i'^* \tag{21}$$

with

$$a_i = \frac{2(f_i^* - f_{i+1}^*)}{(x_{i+1} - x_i)^3} + \frac{f_i'^* + f_{i+1}'^*}{(x_{i+1} - x_i)^2}, \tag{22}$$

$$b_i = \frac{3(f_{i+1}^* - f_i^*)}{(x_{i+1} - x_i)^2} - \frac{2f_i'^* + f_{i+1}'^*}{(x_{i+1} - x_i)} \tag{23}$$

and $X = x - x_i$ are used for f^* and f'^*, respectively.

The equation system is solved on a fixed, inhomogeneous grid with increasing resolution towards the cathode so that $(x_{i+2} - x_{i+1})/(x_{i+1} - x_i) = 1.01$. The time step is chosen so that the Courant–Lewy–Friedrichs criterion $|v_s \Delta t/(x_{i+1} - x_i)| < 0.5$ is fulfilled for the energy density and all particle densities in all grid cells.

4. Results and discussion

The measurements were performed in a xenon pressure range between 0.1 and 5 bar. The applied voltage increase in the outer circuit $\mathrm{d}U/\mathrm{d}t$ was varied between slow (5 mV ns^{-1}) and fast (100 V ns^{-1}) voltage rises.

The high speed photography showed that for all lamps and pressures a volume breakdown occurs. Short time records using the framing camera suggest that for pressures above 0.5 bar only streamers arise. Their size and temporal development was investigated. To get a better understanding of the basic processes the model described above was applied to the experimental conditions. In this section model solutions are discussed in detail and compared with the corresponding experimental results.

4.1. Model results

For comparison between model and experiment appropriate values for the stray capacity C and the effective surface A of the lamp have to be chosen. The stray capacity of the wiring in the experimental set-up can be estimated by the capacity of a Lecher line with wire diameter d of 2 mm, wire separation a of 5 mm and a length of 1 m giving $C_{\mathrm{Lecher}} = \pi\epsilon_0/\mathrm{acosh}(a/d) = 1.8 \times 10^{-11}$ F. On this basis, $C = 1 \times 10^{-11}$ F is chosen as model stray capacitance.

The lamp surface A has to be between the electrode cross-section 2×10^{-7} m^2 and the inner lamp cross-section 4.5×10^{-4} m^2. Approximating the electrode geometry by two spheres with radius $r = 0.25$ mm and separation $d = 5$ mm gives a capacity $C = 2\pi\epsilon_0 r(r + d)/d$ of 1.5×10^{-14} F. A parallel-plate capacitor with identical capacity and plate separation has a surface of 8.3×10^{-6} m^2. Here, $A = 1 \times 10^{-4}$ m^2 is chosen leading to $C_{\mathrm{lamp}} = 1.8 \times 10^{-13}$ F. Model calculations were also done for $A = 10^{-6}$ and 10^{-4} m^2 giving qualitatively identical results as discussed below.

Homogeneous initial particle and energy densities were chosen with $n_\mathrm{e} = 1 \times 10^8$ m^{-3}, $n_\mathrm{i} = 1 \times 10^{12}$ m^{-3}, $n_\mathrm{m} = 0$ and $u_\mathrm{e} = 2\,\mathrm{eV} \times n_\mathrm{e}$. Following the equation for secondary electron emission the electron density at the cathode assumes a value approximately four orders of magnitude below n_i immediately after the start of the model. Consequently, for initial density profiles with $n_\mathrm{e} = n_\mathrm{i}$, a strong electron density gradient forms near the cathode. In order to avoid numerical instabilities associated with this gradient an initial electron density close to the value $\gamma(b_\mathrm{i} n_\mathrm{i} + b_\mathrm{m} n_\mathrm{m})/b_\mathrm{e}$ given by the equation for secondary electron emission was chosen.

Setting $U_0 = 30$ kV in the model ensures breakdown even at a pressure of 5 bar. R is chosen according to (13) so that the intended initial voltage rate $\mathrm{d}U/\mathrm{d}t$ is achieved.

Figures 8–11 show the results for the case $p = 1$ bar and $\mathrm{d}U/\mathrm{d}t = 100$ V ns^{-1} which is chosen as reference case. First, the results for this case are discussed in detail, and then the influence of p and $\mathrm{d}U/\mathrm{d}t$ on the breakdown is investigated.

The general behaviour of the potential and the electron density is similar to that reported in e.g. [5, 30]. It can be divided into three phases: First, an electron avalanche phase where the space charge density does not influence the potential; second, the propagation of an ionization front, and third, the formation of a cathode sheath. During the avalanche phase, the electrons drift towards the anode and ionize the background gas so that electron and ion densities increase with time and distance from the cathode. Ions accumulate due to their small transport coefficients and corresponding small velocities. For the reference case the avalanche phase ends after about 132 ns when the positive space charge imposes a curvature on the potential via Poisson's equation and initiates an ionization front.

Figure 8 shows voltage U, circuit current I and the contributions to I due to electrons $I_\mathrm{e} = eA\Gamma_\mathrm{e}$ and due to the displacement current $I_\mathrm{dis} = -\epsilon_0 A \partial E/\partial t$ at the anode and the velocity v of the ionization front as functions of time. During the avalanche phase the circuit current I is carried mainly by the displacement current. With the onset of field compression I_dis changes its sign, and the electron current I_e after having gone

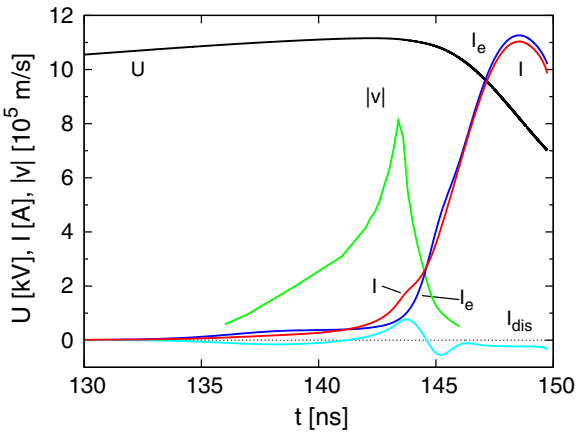

Figure 8. Model results: waveforms of the lamp voltage U, total current I, displacement current I_{dis} and electron current I_{e} at the anode and velocity v of the space charge maximum for $p = 1$ bar, $\mathrm{d}U/\mathrm{d}t = 100\,\mathrm{V\,ns^{-1}}$.

through an exponential increase in the avalanche phase starts to form a plateau. The voltage maximum of 11 kV is reached at around 142 ns. Due to the electric field remaining on the anode side of the ionization front, the electron density increases even after the voltage maximum is passed. The increase in n_{e} in combination with the decrease in the electric field causes I_{e} to reach a maximum of 11.1 A at 148 ns. This maximum current is of the same order as the experimentally obtained maximum current.

The behaviour of the electric field and the electron density during the propagation of the ionization front is illustrated in figure 9. The positive space charge in the ionization front leads to field compression, that is an increase in $|E|$ on the cathode side of the front and a decrease in $|E|$ on its anode side. The increase in $|E|$ between the cathode and the front enhances the local ionization rate so that the point where the space charge influences the potential moves closer to the cathode leading to a further increase in $|E|$. This mechanism leads to the propagation of the front towards the cathode.

The decrease in the electric field strength on the anode side of the ionization front turns the gradient of the electron flux negative so that the space charge density first starts to decrease and then becomes negative at $x \approx 3$ mm and $t \approx 142$ ns. The region with negative space charge forming around this point and its cathode side boundary correspond to the region with negative ∇E and to the maximum of E, respectively. The negative space charge also causes $|E|$ to increase at the anode so that I_{dis} at the anode is positive for times between 141 and 145 ns (cf figure 8).

In a one-dimensional plasma model the total current density is spatially constant. Figure 10 shows the current conservation for $t = 143$ ns. The change in the relevance of displacement and particle currents at the anode with respect to time depicted in figure 8 can be found in figure 10 with respect to space. Between the cathode and the ionization front the total current is carried by the displacement current I_{dis}. In the region between 0.8 and 2.0 mm, where the electric field decreases with time, I_{dis} is negative. Near the anode I_{dis} is again positive corresponding to the observed intermediate increase in $|E|$.

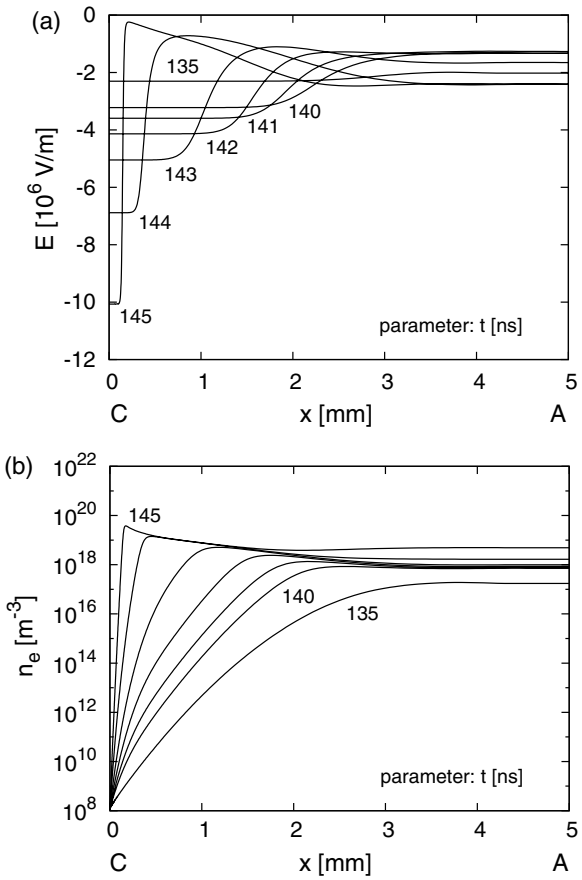

Figure 9. Model results: electric field E (a) and electron density n_{e} (b) during the propagation of the ionization front for $p = 1$ bar, $\mathrm{d}U/\mathrm{d}t = 100\,\mathrm{V\,ns^{-1}}$.

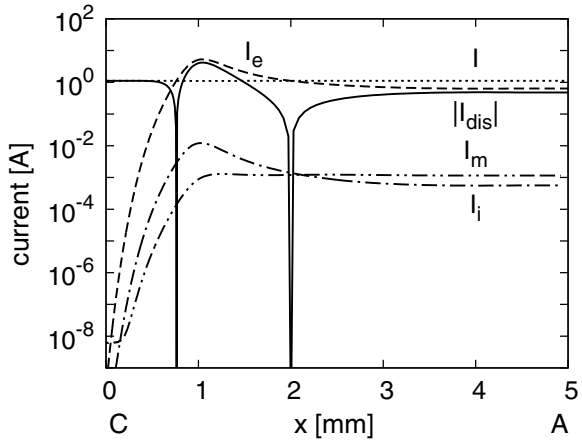

Figure 10. Model results: currents I_{e}, I_{i} and I_{m} due to electrons, Xe^+ ions and Xe_2^+ ions, respectively, displacement current I_{dis} and total current I at $t = 143$ ns for $p = 1$ bar, $\mathrm{d}U/\mathrm{d}t = 100\,\mathrm{V\,ns^{-1}}$. I_{dis} is negative in the interval from 0.8 to 2.0 mm and positive otherwise.

For $x \geqslant 0.2$ mm the ion currents $I_{\mathrm{i}} = eA\Gamma_{\mathrm{i}}$ and $I_{\mathrm{m}} = eA\Gamma_{\mathrm{m}}$ are typically two to three orders of magnitude smaller than I_{e}. In the ionization front I_{i} exceeds I_{m} because the ionization rate is larger than the conversion rate here. The secondary electron emission at the cathode is mainly driven by Xe_2^+ ions. These ions were created from Xe^+ ions by conversion reactions in three-body collisions.

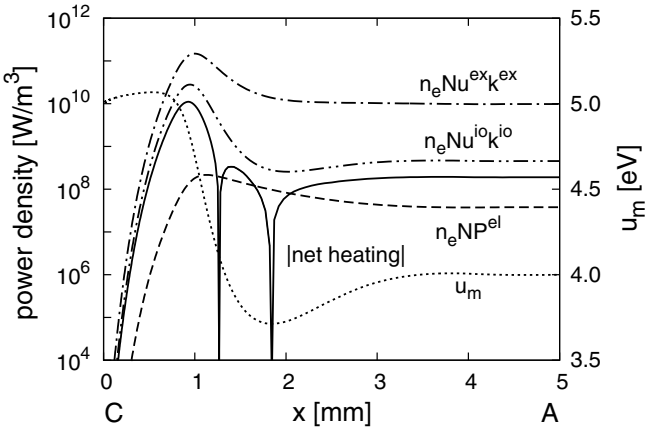

Figure 11. Model results: net heating and loss terms in the electron energy balance at $t = 143$ ns for $p = 1$ bar, $\mathrm{d}U/\mathrm{d}t = 100\,\mathrm{V\,ns^{-1}}$. The electron fluid cooled in the interval from 1.3 to 1.8 mm and heated otherwise.

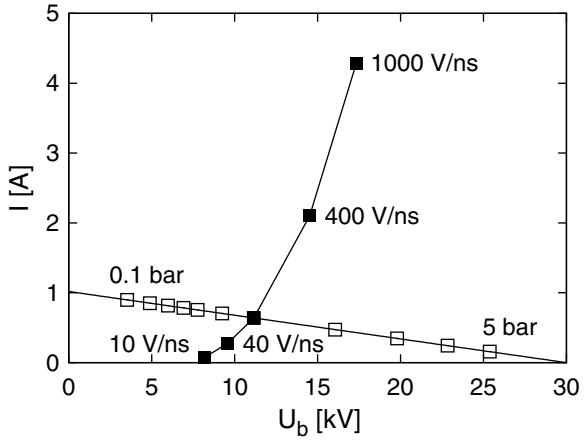

Figure 12. Model results: circuit currents I at breakdown voltages U_b for constant voltage increase $\mathrm{d}U/\mathrm{d}t = 100\,\mathrm{V\,ns^{-1}}$ (□) and constant pressure $p = 1$ bar (■). The pressures for constant $\mathrm{d}U/\mathrm{d}t$ are 0.1, 0.2, 0.3, 0.4, 0.5, 0.7, 1, 2, 3, 4 and 5 bar.

Figure 11 shows the energy loss channels and the net heating acting in the electron energy balance equation and the mean electron energy u_m at $t = 143$ ns. It is found that except close to the cathode the energy balance is fulfilled by a local balance of ohmic heating and collisional losses. Heating and losses differ by less than 10% and 2% on the cathode and the anode side of the ionization front, respectively. The electron gas is heated everywhere except in the region between 1.3 and 1.8 mm where it is cooled. In general the contributions of ionization, excitation and elastic losses to the total energy loss are functions of the local mean electron energy u_m. For $t = 143$ ns the mean electron energy exceeds 2.6 eV at each position so that excitation is the dominant loss channel representing more than 78% of the total energy loss. As u_m exceeds 3.5 eV everywhere in the plasma at 143 ns the remaining losses are caused by ionization (cf figure 6(*a*)).

For times $t < 143$ ns the inertia terms of the energy balance equation represent less than 10% of the ohmic heating. This indicates that the electrons are well in equilibrium with the local electric field. A corresponding observation is the small relaxation length of u_m near the cathode. After starting with 2 eV at the cathode, u_m needs approximately only 5×10^{-6} m to relax to the value $u_\mathrm{m}(E/N)$ given by the solution of the homogeneous Boltzmann equation for the electrons. Thus the local field approximation may be applied in the early phase of the propagation of the ionization front. However, at later times the inertia terms of the energy balance are important both on the cathode side of the ionization front and in the bulk plasma. As long as the inertia terms of the energy balance equation are small with respect to the heating term, the mean electron energy u_m closely follows the value $u_\mathrm{m}(E/N)$ shown in figure 6(*a*).

In order to test the influence of the initial densities on the model results, calculations with $n_\mathrm{e} = 1 \times 10^6$ and $1 \times 10^7\,\mathrm{m^{-3}}$, $n_\mathrm{i} = 10^4\,n_\mathrm{e}$ for the reference case were performed. The results were qualitatively identical to those with $n_\mathrm{e} = 1 \times 10^8\,\mathrm{m^{-3}}$. Decreasing n_e from 1×10^8 to $1 \times 10^6\,\mathrm{m^{-3}}$ led to a delay of the breakdown by 7 ns, an increase in U_b by approximately 400 V, a shift of the ionization front 0.2×10^{-3} m towards the anode and an increase in the current maximum by 18%.

As the ion density at the time of formation of the ionization front exceeds the initial ion density by several orders of magnitude, the value of n_i in the volume was expected to have only a small influence on the model results. This was tested by a model calculation with a box-shaped initial ion density profile $n_\mathrm{i} = 1 \times 10^{12}\,\mathrm{m^{-3}}$ for $x \leqslant 0.2 \times 10^{-3}$ m and $n_\mathrm{i} = n_\mathrm{e} = 1 \times 10^8\,\mathrm{m^{-3}}$ else. The results were found to be identical to those of the reference case.

The influence of the surface A was investigated by performing model calculations with $A = 10^{-5}$ and $10^{-6}\,\mathrm{m^2}$. The results were similar to those of the reference case. The reduction in A from 1×10^{-4} to $1 \times 10^{-6}\,\mathrm{m^2}$ led to a delay of the breakdown by 7 ns and an increase in U_b by approximately 500 V. Consequently, the chosen circuit parameters and initial conditions represent an appropriate choice.

The following paragraphs consider the dependence of the breakdown voltage U_b on the voltage rise $\mathrm{d}U/\mathrm{d}t$ and on pressure p. Figure 12 shows the circuit current at breakdown as a function of U_b for pressures from 0.1 to 5 bar at constant rise time $\mathrm{d}U/\mathrm{d}t = 100\,\mathrm{V\,ns^{-1}}$ and for rise times from 40 to $1000\,\mathrm{V\,ns^{-1}}$ at constant pressure $p = 1$ bar. As U_b is the maximum value of the lamp voltage, and $\dot{U}(t)$ vanishes at breakdown, circuit equation (9) leads to

$$U_\mathrm{b} = U_0 - RI = U_0\left[1 - I\left(C_0\mathrm{d}U/\mathrm{d}t\right)^{-1}\right]. \qquad (24)$$

Relation (13) has been used to obtain the right-hand side of (24). Thus, for constant voltage rate $\mathrm{d}U/\mathrm{d}t$, I is a linear function of U_b. According to (24) the maximum possible current at breakdown for $\mathrm{d}U/\mathrm{d}t = 100\,\mathrm{V\,ns^{-1}}$ is $I_{\mathrm{b,max}} = C_0(\mathrm{d}U/\mathrm{d}t) = 1.02$ A. For given $\mathrm{d}U/\mathrm{d}t$, $I_{\mathrm{b,max}}$ is determined by the choice of the stray capacity C. The model results shown in figure 12 fulfil (24) and show that high currents I are reached at low U_b and low pressures.

The model results for constant pressure show an increase in the breakdown voltage U_b with increasing $\mathrm{d}U/\mathrm{d}t$. According to (24) the breakdown voltage would stay constant if the current I at breakdown rose by the same factor as $\mathrm{d}U/\mathrm{d}t$. Figure 12 shows that I increases with growing $\mathrm{d}U/\mathrm{d}t$,

however, not enough to hold U_b constant. Increasing dU/dt from e.g. 100 to 1000 V ns^{-1} gives a rise of I by a factor of only 6.7. Even though the displacement current contributes to the total current at the anode, one may understand this behaviour considering the electron density. The electron density on the anode side of the ionization front follows $n_e(t) = n_{e0} \exp[N \int_0^t k^{io}(t')dt']$. When dU/dt is increased, U reaches its former breakdown value U_b in a shorter period of time, so that n_e cannot attain its former value and the current is yet too small to cause the breakdown. Consequently, U surpasses the former U_b, so that U_b increases with growing dU/dt.

Figure 13 shows the velocity of the space charge maximum versus its distance to the cathode x for various pressures and voltage rises. The model results show an acceleration of the front at large distances and a decrease in the front speed in the vicinity of the cathode. As shown in figure 8 the front velocity increases before and sinks after the lamp voltage has reached its maximum, respectively. The maximum velocities are in the range from 2×10^5 to 2×10^6 m s^{-1}. They are of the same order as those reported by Beckers *et al* [6] and Sobota *et al* [9]. In agreement with these authors the front velocity increases with increasing voltage rise dU/dt and decreasing pressure p. An initial acceleration of the front towards the cathode was also obtained by Sobota *et al* [9] in measurements of the velocity of streamers along a dielectric surface.

In model calculations employing a smaller stray capacity C of 10^{-13} F the buildup of negative space charge on the anode side of the ionization front led to the formation of a region with a reversed, positive electric field. The reversal of the electric field is a known phenomenon in low pressure dc glow discharges and was investigated by experiments in e.g. [45] and by numerical modelling in e.g. [46]. However, a region with negative space charge and a field reversal was not observed in the two-dimensional simulations of the breakdown of HID lamps reported in [3, 5]. The appearance of a negative space charge region for particular choices of the circuit parameters may be due to the absence of the radial electron flux in this model while it is naturally included in two-dimensional models. Using $n_e = 10^{17}$ m^{-3}, $E = -1.5$ MV m^{-1}, and $r = 0.25 \times 10^{-3}$ m as radius of the plasma channel one may estimate a radial electron flux $D_e n_e / r$ of 4×10^{19} m^{-2} s^{-1} and an axial electron flux $-b_e n_e E$ of 4×10^{21} m^{-2} s^{-1}. Considering the high aspect ratio of the plasma channel in the experiment the radial electron flux may contribute significantly to the electron continuity equation.

It can be concluded that the model can well describe the breakdown of the lamp voltage and the early phase of the propagation of the ionization front. A quantitative model of the further temporal development of the breakdown and the transition to a thermionic arc requires the consideration of radial losses and ionization from excited and molecular states.

4.2. Experimental results and comparison with model calculations

The measurements show that for all lamps with pressures between 0.1 and 5 bar a volume breakdown occurs. Short

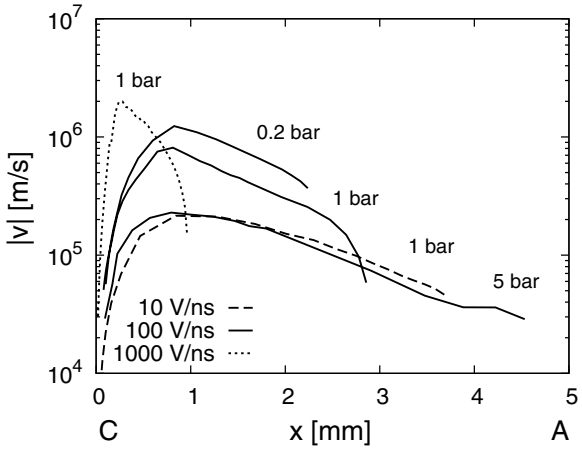

Figure 13. Model results: velocity of the ionization front v versus the position x of the space charge maximum for voltage rises of 10 V s^{-1} at 1 bar (----), 100 V s^{-1} at 0.2, 1 and 5 bar (——), and 1000 V ns^{-1} (– – –) at 1 bar.

time records taken by the framing camera suggest that a diffuse breakdown does not occur for pressures above 0.5 bar. Instead only streamers arise then. The streamers show strong branching at the anode side of the lamp (see figure 3). Their spatial structure seems to be independent of the xenon pressure.

In lamps with xenon pressures from 1 to 5 bar a dark region in front of the cathode was observable. Its spatial extension remained constant during the temporal development of the breakdown. This behaviour was found for both slow ($dU/dt = 0.4$ V ns^{-1}) and fast ($dU/dt = 100$ V ns^{-1}) voltage rises. The dark area in front of the cathode decreased its size with rising pressure and additional UV radiation.

While the UV radiation has no visible influence on the streamer shape at higher pressures it changes the diffuse breakdown channel observed for pressures up to 0.3 bar into a constricted one. This behaviour is shown in figure 14. A similar constriction for ac ignitions with high frequencies was reported by Beckers *et al* [6]. While in the experiments of Beckers *et al* this transition may be due to residual electrons it is caused by photoelectrons emitted by the electrodes in this study.

In figure 15 the lamp breakdown voltage is plotted as a function of the xenon pressure for values from 0.1 to 5 bar and a voltage rise time of $dU/dt = 100$ V ns^{-1}. The results show an increase in the breakdown voltage with rising xenon pressure. Theoretical values of the breakdown voltages were taken from voltage waveforms as shown in figure 8. Experimental and modelling results show good agreement. The breakdown voltage increases with growing pressure because a smaller reduced electric field E/N leads to a smaller mean electron energy u_m (figure 6). A reduced mean electron energy leads in turn to a smaller ionization frequency Nk^{io} so that a current sufficient to cause the breakdown is reached at later times and consequently higher voltages.

At pressures below 0.5 bar diffuse breakdown was found. An overview of experimentally determined breakdown voltages for a Townsend breakdown of xenon was presented by Hess [47]. It is known that the Townsend theory for breakdown is valid for discharges where the product pd of pressure and

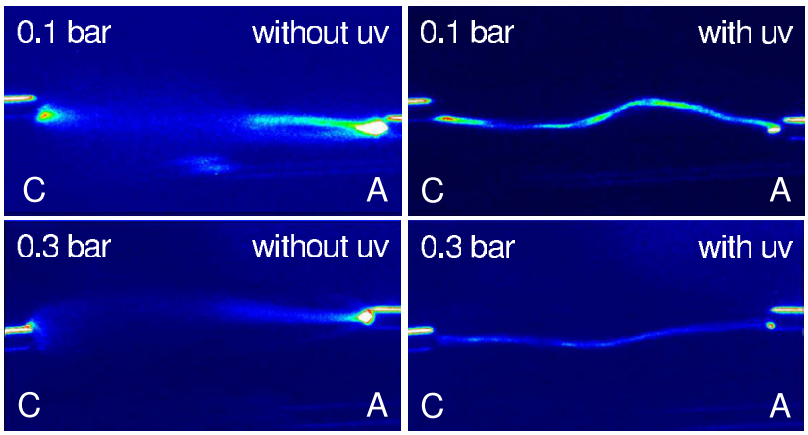

Figure 14. Discharge channel for xenon pressures of 0.1 and 0.3 bar with and without additional UV radiation. UV radiation leads to constricted discharge channels.

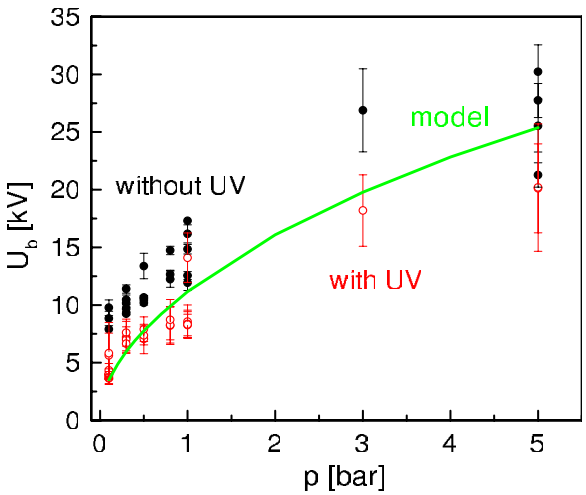

Figure 15. Comparison of model (——) and experimental breakdown voltages with (○) and without (●) additional UV radiation as a function of the xenon pressure for $dU/dt = 100\,V\,ns^{-1}$.

electrode gap has values less than 100 Torr cm. For *pd* values larger than 400 Torr cm, corresponding to pressures above approximately 1 bar in the present experiments, the extrapolated values given in [47] exceed the measured breakdown voltages even though the results in [47] do not account for the impedance of the power supply. The reason for this difference is the occurrence of the streamer breakdown in this study. In the model the field compression and the subsequent streamer-like, cathode-directed ionization front are initiated before the first secondary electrons have crossed the electrode gap.

Additional UV background radiation reduces the breakdown voltage of lamps by up to 5 kV as illustrated in figure 15. For pulsed ignition a similar reduction in the breakdown voltage was reported by Beckers *et al* [6]. The mercury lamp employed here as UV source emits radiation at a wavelength of 254 nm corresponding to a photon energy of 4.66 eV. This energy is too small to ionize xenon in its ground state, but high enough to force the tungsten electrodes having a work function of 4.55 eV to emit photoelectrons. Xenon metastable states can also be ionized by the applied UV radiation; however, xenon metastable states are rapidly converted to Xe_2^* molecules in three-body collisions with Xe as shown in [30]. With an ionization energy of 11.1 eV Xe_2^* molecules are not liable to photoionization in this experiment. Experiments with a spatially limited illumination of parts of the gas volume between the electrodes showed correspondingly no influence on the breakdown voltage. The observed reduction in the breakdown voltage is thus due to UV illumination of the electrodes.

A comparison of experimental and model breakdown voltages U_b as a function of the voltage rise dU/dt for $p = 1$ bar is shown in figure 16. Theoretical values of the breakdown voltage were taken from voltage waveforms as shown in figure 8. The breakdown voltage increases with increasing voltage rise. Figure 16 shows good agreement between experimental and theoretical results for voltage rises in the range provided by commercially applied ignition devices.

Beckers *et al* [6] investigated breakdown in xenon lamps for the two pressures 0.3 and 0.7 bar and voltages pulsed at $1000\,V\,ns^{-1}$. They found breakdown voltages above those reported here for both pressures. As the voltage rises at $100\,V\,ns^{-1}$ in the present experiments, this difference is in good agreement with the fact that U_b increases with dU/dt.

5. Conclusions

Breakdown voltages were determined theoretically and experimentally for streamer breakdown in xenon at high pressure. The breakdown voltage could be decreased by additional illumination of the lamp electrodes with UV radiation. The breakdown voltage increases with increasing pressure and growing rate of increase in the applied voltage. Both these findings can be explained by model calculations. The employed fluid model gives breakdown voltages in good agreement with the experiments. In the model the accumulation of positive space charge initiates a cathode-directed ionization front. Positive feedback of increased ionization rate and field compression leads to an accelerated propagation of the ionization front towards the cathode until

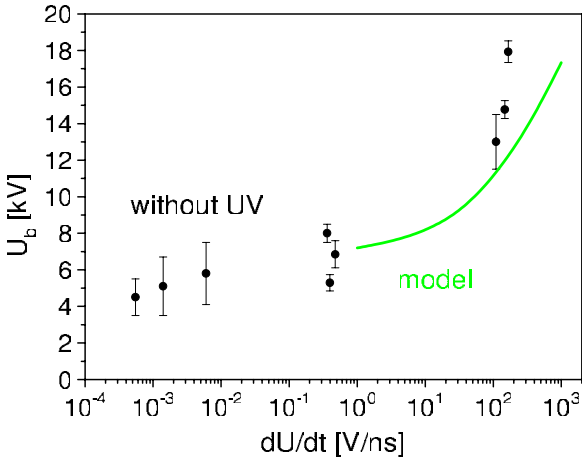

Figure 16. Comparison of model (——) and experimental breakdown voltages without (●) additional UV radiation as a function of the voltage rise dU/dt for $p = 1$ bar.

the lamp voltage U drops due to the increasing circuit current. While photoionization can play a role in the experiment the ionization front obtained in the model propagates without it. However, the front in the model relies on the existence of ions near the cathode so that secondary electrons can initiate electron avalanches.

Acknowledgments

The authors would like to thank S Hadrath for first measurements and OSRAM GmbH for manufacturing the lamps. This work was supported in part by the German Federal Ministry for Education and Research (BMBF, FKZ 13N8604).

References

[1] Born M 2001 Investigations on the replacement of mercury in high-pressure discharge lamps by metallic zinc *J. Phys. D: Appl. Phys.* **34** 909–24

[2] Grundmann D, Schimke C, Reiners T and Hering O 2003 Hg-free gas discharge lamps for automotive use *Proc. 5th Int. Symp. on Progress in Automobile Lighting (Darmstadt)* vol 10 (München: Herbert Utz) pp 351–64

[3] Lay B, Moss R S, Rauf S and Kushner M J 2003 Breakdown processes in metal halide lamps *Plasma Sources Sci. Technol.* **12** 8–21

[4] Moss R S, Eden J G and Kushner M J 2004 Avalanche processes in an idealized lamp: I. Measurements of formative breakdown time *J. Phys. D: Appl. Phys.* **37** 2502–09

[5] Bhoj A N and Kushner M J 2004 Avalanche processes in an idealized lamp: II Modelling of breakdown in Ar/Xe electric discharges *J. Phys. D: Appl. Phys.* **37** 2510–26

[6] Beckers J, Manders F, Aben P C H, Stoffels W W and Haverlag M 2008 Pulse, dc and ac breakdown in high pressure gas discharge lamps *J. Phys. D: Appl. Phys.* **41** 144028

[7] Raizer Yu P 1991 *Gas Discharge Physics* (Berlin: Springer)

[8] Czichy M, Hartmann T, Mentel J and Awakowicz P 2008 Ignition of mercury-free high intensity discharge lamps *J. Phys. D: Appl. Phys.* **41** 144027

[9] Sobota A, Lebouvier A, Kramer N J, van Veldhuizen E M, Stoffels W W, Manders F and Haverlag M 2009 Speed of streamers in argon over a flat surface of a dielectric *J. Phys. D: Appl. Phys.* **42** 015211

[10] Brok W J M, van Dijk J, Bowden M D, van der Mullen J J A M 2003 A model study of propagation of the first ionization wave during breakdown in a straight tube containing argon *J. Phys. D: Appl. Phys.* **36** 1967–79

[11] Meyyappan M, Kreskovsky J P 1990 Glow discharge simulation through solutions to the moments of the Boltzmann transport equation *J. Appl. Phys.* **68** 1506–12

[12] Elaissi S, Yousfi M, Charrada K and Troudi L 2005 Electric discharge fluid modelling with contribution of convective and drift energy effects *Eur. Phys. J. Appl. Phys.* **32** 37–44

[13] Li C, Brok W J M, Ebert U and van der Mullen J J A M 2007 Deviations from the local field approximation in negative streamer heads *J. Appl. Phys.* **101** 123305

[14] Ducasse O, Papageorghiou L and Eichwald O 2007 Critical analysis on two-dimensional point-to-plane streamer simulations using the finite element and finite volume methods *IEEE Trans. Plasma Sci.* **35** 1287–300

[15] Ebert U, van Saarloos W and Caroli C 1997 Propagation and structure of planar streamer fronts *Phys. Rev.* E **55** 1530–49

[16] Kulikovsky A A 2000 The role of photoionization in positive streamer dynamics *J. Phys. D: Appl. Phys.* **33** 1514–24

[17] Panchesnyi S V, Starikovskaja S M and Starikovskii A Y 2001 Role of photoionization processes in propagation of cathode-directed streamers *J. Phys. D: Appl. Phys.* **34** 105–15

[18] Arrayás M, Fontelos M A and Trueba J L 2006 Photoionization effects in ionization fronts *J. Phys. D: Appl. Phys.* **39** 5176–82

[19] Luque A, Ratushnaya V and Ebert U 2008 Positive and negative streamers in ambient air: modelling evolution and velocities *J. Phys. D: Appl. Phys.* **41** 234005

[20] Rocco A, Ebert U and Hundsdorfer W 2002 Branching of negative streamers in free flight *Phys. Rev.* E **66** 035102(R)

[21] Montijn C, Ebert U and Hundsdorfer W 2006 Numerical convergence of the branching time of negative streamers *Phys. Rev.* E **73** 065401(R)

[22] Pancheshnyi S V, Sobakin S V, Starikovskaya S M and Starikovskii A Y 2000 Discharge dynamics and the production of active particles in a cathode-directed streamer *Plasma Phys. Rep.* **26** 1054–65

[23] Eichwald O, Ducasse O, Dubois D, Abahazem A, Merbahi N, Benhenni M and Yousfi M 2008 Experimental analysis and modelling of positive streamer in air: towards an estimation of O and N radial production *J. Phys. D: Appl. Phys.* **41** 234002

[24] Ebert U and Sentman D D 2008 Streamer, sprites, leaders, lightning: from micro- to macroscales *J. Phys. D: Appl. Phys.* **41** 230301

[25] Stenbaek-Nielsen H C and McHarg M G 2008 High time-resolution sprite imaging: observations and implications *J. Phys. D: Appl. Phys.* **41** 234009

[26] Briels T M P, Kos J, van Veldhuizen E M and Ebert U 2006 Circuit dependence of the diameter of pulsed positive streamers in air *J. Phys. D: Appl. Phys.* **39** 5201–10

[27] Briels T M P, Kos J, Winands G J J, van Veldhuizen E M and Ebert U 2008 Positive and negative streamers in ambient air: measuring diameter, velocity and dissipated energy *J. Phys. D: Appl. Phys.* **41** 234004

[28] Yabe T and Aoki T 1991 A universal solver for hyperbolic equations by cubic-polynomial interpolation: I. One-dimensional solver *Comput. Phys. Commun.* **66** 219–32

[29] Utsumi T, Kunugi T and Aoki T 1997 Stability and accuracy of the cubic interpolated propagation scheme *Comput. Phys. Commun.* **101** 9–20

[30] Carman R J and Mildren R P 2003 Computer modelling of a short-pulse excited dielectric barrier discharge xenon

excimer lamp ($\lambda \sim 172$ nm) *J. Phys. D: Appl. Phys.* **36** 19–33
[31] Bogdanov E A, Kudryavtsev A A, Arsanbelkov R R and Kolobov V I 2004 Simulation of pulsed dielectric barrier discharge xenon excimer lamp *J. Phys. D: Appl. Phys.* **37** 2987–95
[32] Gortchakov S and Uhrlandt D 2005 Radiation properties of low-pressure discharges in rare-gas mixtures containing xenon *Plasma Sources Sci. Technol.* **14** 177–83
[33] Graves D B and Jensen K F 1986 A continuum model of dc and rf discharges *IEEE Trans. Plasma Sci.* **14** 78–91
[34] Graves D B 1987 Fluid model simulations of a 13.56-MHz RF discharge—time and space dependence of rates of electron-impact excitation *J. Appl. Phys.* **62** 88–94
[35] Richards A D, Thompson B E and Sawin H H 1987 Continuum modelling of argon radio frequency glow-discharge *Appl. Phys. Lett.* **50** 492–4
[36] Gogolides E, Nicolai J P and Sawin H H 1989 Comparison of experimental measurements and model predictions for radio-frequency Ar discharges and SF_6 discharges *J. Vac. Sci. Technol.* **7** 1001–6
[37] Boeuf J P and Pitchford L C 1995 Two-dimensional model of a capacitively coupled rf discharge and comparison with experiments in the gaseous electronics conference reactor *Phys. Rev.* E **51** 1376–90
[38] Viehland L A and Mason E A 1995 Transport properties of gaseous ions over a wide energy range *At. Data Nucl. Data Tables Part IV* **60** 37–95
[39] Leyh H, Loffhagen D and Winkler R 1998 A new multi-term solution technique for the electron Boltzmann equation of weakly ionized steady-state plasmas *Comput. Phys. Commun.* **113** 33–48
[40] Pinhao N R, Donkó Z, Loffhagen D, Pinheiro M J and Richley E A 2004 Comparison of kinetic calculation techniques for the analysis of electron swarm transport at low to moderate E/N values *Plasma Sources Sci. Technol.* **13** 719–28
[41] Hayashi M 1990 *Nonequilibrium Processes in Partially Ionized Gases* ed M Capitelli and J N Bardley (New York: Plenum) pp 333–40
[42] Rapp D and Englander-Golden P 1965 Total cross sections for ionization and attachment in gases by electron impact: I. Positive ionization *J. Comput. Phys.* **43** 1464–79
[43] Puech V and Mizzi S 1991 Collision cross sections and transport parameters in neon and xenon *J. Phys. D: Appl. Phys.* **24** 1974–85
[44] Fletcher C A F 1991 *Computational Techniques for Fluid Dynamics* 2nd edn (Berlin: Springer)
[45] Gottscho R A, Mitchel A, Scheller G R and Chan Y 1989 Electric field reversals in dc negative glow discharges *Phys. Rev.* A **40** 6407–14
[46] Loffhagen D, Sigeneger F and Winkler R 2004 The effect of a field reversal on the spatial transition of the electrons from an active plasma to a field-free remote plasma *Eur. Phys. J. Appl. Phys.* **25** 45–56
[47] Hess H 1976 *Der elektrische Durchschlag in Gasen* (Berlin: Akademie) p 67